Quantifying viscosity and surface tension of multicomponent protein-nucleic acid condensates

Ibraheem Alshareedah,[1] George M. Thurston,[2] and Priya R. Banerjee[1],*
[1]Department of Physics, University at Buffalo SUNY, Buffalo, New York and [2]School of Physics and Astronomy, Rochester Institute of Technology, Rochester, New York

ABSTRACT   Living cells organize their internal space into dynamic condensates through liquid-liquid phase separation of multivalent proteins in association with cellular nucleic acids. Here, we study how variations in nucleic acid (NA)-to-protein stoichiometry modulate the condensed phase organization and fluid dynamics in a model system of multicomponent heterotypic condensates. Employing a multiparametric approach comprised of video particle tracking microscopy and optical tweezer-induced droplet fusion, we show that the interfacial tension, but not viscosity, of protein-NA condensates is controlled by the NA/protein ratio across the two-phase regime. In parallel, we utilize fluorescence correlation spectroscopy to quantify protein and NA diffusion in the condensed phase. Fluorescence correlation spectroscopy measurements reveal that the diffusion of the component protein and NA within the condensate core is governed by the viscosity, and hence, also remains insensitive to the changes in NA-to-protein stoichiometry. Collectively, our results provide insights into the regulation of multicomponent heterotypic liquid condensates, reflecting how the bulk mixture composition affects their core versus surface organization and dynamical properties.

SIGNIFICANCE   A quantitative study of the organization and dynamical properties of biomolecular liquid condensates requires the integration of experimental methodologies from soft matter physics and quantitative optical microscopy. In this letter, we employ a multiparametric approach to quantify viscosity, surface tension, and macromolecular diffusion of multicomponent protein-nucleic acid condensates by combining particle tracking microrheology, optical tweezer-induced droplet fusion, and fluorescence correlation spectroscopy. Our measurements of viscosity, surface tension, and diffusion shed light on the organization of the condensate core, the architecture of the condensate surface, and the protein and nucleic acid diffusion in the dense phase.

INTRODUCTION

Ribonucleoprotein (RNP) granules, such as stress granules, P bodies, and nucleoli, are fluid-like subcellular condensates formed through liquid-liquid phase separation of multivalent proteins in association with cellular nucleic acids (1,2). It is now well appreciated that these condensates carry essential intracellular functions as signaling hubs and storage compartments (3,4), and are conserved from bacteria to humans (5–7). The biophysical properties of cellular protein-nucleic acid (NA) condensates, such as molecular composition, surface tension, viscosity, and macromolecular diffusion, are important determinants of their cellular functions, whereas alterations in the same have been linked

to various disease pathologies, such as neurological disorders and certain types of cancer (8–11). Many of the pathological variants of cellular biomolecular condensates usually display altered condensate network structure and composition, which is believed to cause either a loss-of-function or a gain-in-toxicity phenotype (12–14).

Although many cellular NA-binding proteins can undergo homotypic condensation, heterotypic interactions with NAs constitute an important mode of regulation in this process (15–17). Recent evidence suggests several regulatory roles of cellular NAs in the formation of nucleoprotein granules, such as condensate-nucleating scaffolds (18,19), and in the autoregulation of RNP condensation through a reentrant phase transition (20,21). The RNA-mediated reentrant phase transition is marked by condensation and a subsequent decondensation of RNPs in response to increasing the RNA/protein mixing ratio (22). In addition, variations in mixture composition within the two-phase regime can produce distinct morphological transitions, such as the formation

of hollow vesicle-like condensates in a binary protein-RNA mixture (23). These observations suggest that heterotypic multicomponent interactions are sensitively dependent on protein-NA stoichiometry, pointing to a nontrivial mechanism of composition-dependent condensation in multicomponent mixtures (24).

In this letter, we probe the effect of mixture composition on the viscosity and surface tension of protein-NA condensates. The polymer network structure within a condensate primarily determines the viscosity of the condensate (25). The viscosity directly influences the rate of molecular exchange within the condensate and is dependent on both the intermolecular interactions and the structural features of the constituting biopolymers (25). Surface tension, on the other hand, determines the shape of the condensate as well as its interactions with solid and liquid interfaces and is dependent on the surface composition and charge. To quantify the viscosity and surface tension of protein-NA condensates, we employ a multiparametric approach by combining video particle tracking (VPT) microscopy and optical tweezer-induced droplet fusion (OTF). As a model system, we utilized in vitro reconstituted condensates formed by a positively charged low-complexity disordered polypeptide containing Arg-Gly repeats ([RGRGG]$_5$) and a negatively charged homopolymeric single-stranded DNA (dT40). In parallel to determining viscosity and surface tension, we use fluorescence correlation spectroscopy (FCS) to quantify protein and nucleic acid diffusion in these condensates to explore how alterations in mixture composition impact biomolecular diffusion in the dense phase and how molecular diffusion compares with variations in the viscosity of the liquid condensates. Our results suggest that these heterotypic protein-NA condensates assume spatially organized structures in the mesoscale, in which the condensate surface, but not the condensate core, is responsive to alterations in the bulk mixture stoichiometry.

Results and discussion

A multiparametric approach to quantify molecular diffusion within and material properties of biomolecular condensates

Previously, we and others have demonstrated that OTF of biomolecular condensates provides an improved and sensitive analysis of their fusion speed in vitro (26–28). Because the droplets are trapped in solution, spurious effects from surface drag force, as in the case of passive droplet fusion, are eliminated (29). In this assay, two condensates are trapped optically using a dual-trap optical tweezer coupled with a confocal fluorescence microscope. The optical trapping of the condensates is facilitated by the refractive index mismatch between the condensate and the coexisting dilute phase. The droplet fusion was initiated by the controlled movement of one droplet at a constant velocity toward another stationary droplet (Fig. 1 *A*). By analyzing the laser signal relaxation from the optical traps during the droplet

fusion event, a fusion relaxation timescale τ is extracted (Fig. 1 *B*). For droplets displaying Newtonian fluid properties, this relaxation time is proportional to the ratio of the viscosity η over surface tension γ (30) and can be written as

$$\tau \Big/ l = \frac{\eta}{\gamma}, \tag{1}$$

where l is the average diameter of the fusing droplets. Measurement of inverse capillary velocity (η/γ) alone does not provide any direct information on the viscosity and/or surface tension of condensates, unless an independent assay is used to measure one of these quantities (30). To this end, we employed VPT microscopy, which enables the determination of the viscosity of the same condensates (31). In brief, yellow-green polystyrene beads (200 nm) with carboxylate-modified surfaces (31,32) were passively embedded into these condensates and their motion was tracked using fluorescence VPT (Fig. 1 *C*). The polystyrene beads were premixed with the buffering solution before mixing the peptide and DNA to form condensates. By tracking the Brownian motion of a large number of beads inside the dense phase, we extracted their average mean squared displacement (MSD; Fig. 1 *D*). These MSD plots were used to estimate the diffusion coefficient of polystyrene beads. Subsequently, the condensate viscosity was obtained using the Stokes-Einstein relation (see below). Finally, by combining the measured inverse capillary velocity from the fusion experiments and the measured viscosity from VPT experiments, we used Eq. 1 to obtain the interfacial tension of the condensate.

To quantify the surface tension and viscosity of heterotypic protein-NA condensates, we utilized model condensates formed by a low-complexity Arg-Gly-rich polypeptide [RGRGG]$_5$ and a homopolymeric single-stranded DNA [dT]$_{40}$ (dT40). Before OTF and VPT experiments, we confirmed that the [RGRGG]$_5$-dT40 mixture displayed a reentrant phase behavior by using solution turbidity measurement and fluorescence microscopy with a fixed [RGRGG]$_5$ concentration (5.0 mg/mL) and variable DNA/peptide mixing ratio. The mixture turbidity displayed a peak around a [T]/[Arg] ratio of 0.4 ([nucleotide]:[Arg]) and considerably decreased beyond a ratio of 1.0, indicating that phase separation is maximal (largest number of interfaces and scattering amplitudes) around a [T]/[Arg] ratio of 0.4 (Fig. S1). This is corroborated by the fact that droplets at [T]/[Arg] ratio of 0.4 are significantly larger, and they cover more surface area on the coverslip (~45% as judged by fluorescence microscopy) than those prepared at other mixing ratios (Fig. S1). For oppositely charged polymers, it is intuitive to expect that phase separation is maximal at their formal charge-neutral stoichiometry conditions ([T]/[Arg] = 1). However, this prediction may not hold for peptides and NAs because of a combined effect of uneven local charge distributions on the peptide chain (33), charge
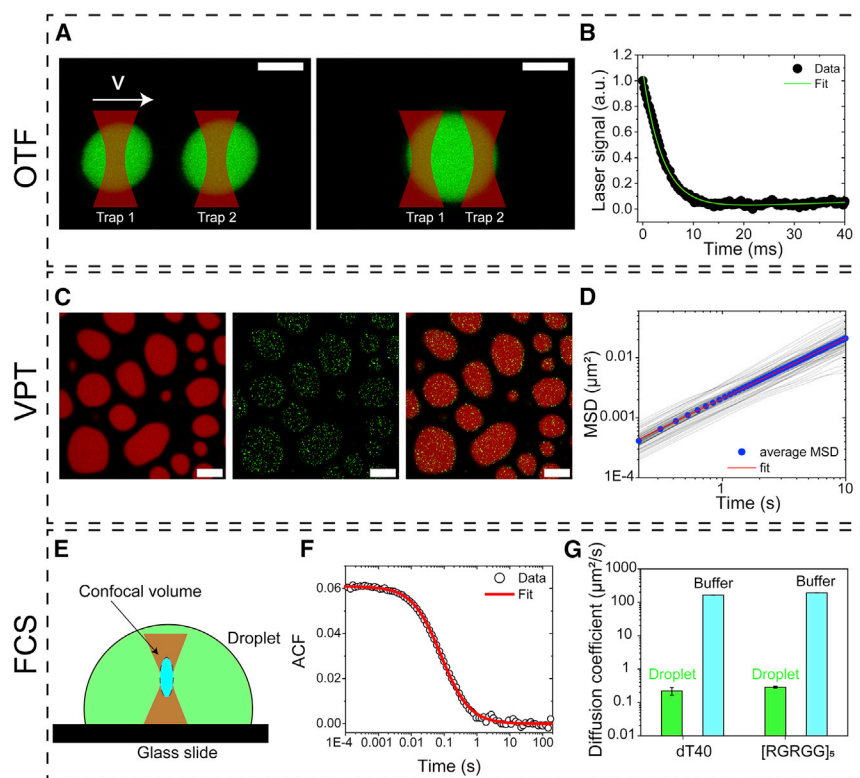
FIGURE 1 A multiparametric approach to quantify material properties of and molecular diffusion within biomolecular condensates. (*A*) Illustration shows optical tweezer-induced droplet fusion (OTF) assay using a dual-trap optical tweezer and correlative time-lapse imaging of condensates using confocal fluorescence microscopy. (*B*) A representative force relaxation curve from our OTF assay that is fitted using an appropriate model (see Supporting materials and methods for details) to extract inverse capillary velocity is shown. (*C*) Illustration is shown of video particle tracking (VPT) microscopy assay that shows fluorescently labeled condensates (*red*) and 200-nm polystyrene beads (*green*) within. Scale bars represent 10 μm. (*D*) MSDs of individual particles (*light shade of gray*) and the corresponding ensemble-averaged MSD (*blue circles*), which is fitted (*red line*) with $MSD = 4Dt^\alpha$ ($\alpha = 1$ for Brownian particles; $D =$ diffusion coefficients of the beads) are shown. These data were obtained by tracking 200-nm beads in dT40-[RGRGG]$_5$ condensates prepared at 0.4 [T]/[Arg] ratio. (*E*) The schematic diagram illustrates the positioning of the confocal volume inside a condensate for fluorescence correlation spectroscopy (FCS) analysis. (*F*) A typical autocorrelation curve for freely diffusing [RGRGG]$_5$ molecules (labeled with Alexa 594) within a condensate is shown. (*G*) A plot summarizing FCS-derived diffusion coefficients of the peptide and DNA molecules in dilute buffer solution and within phase-separated condensates is shown. All error bars represent $\pm$ 1 standard deviation.

regulation effects (34,35), and the presence of short-range non-electrostatic interactions (22).

The [RGRGG]$_5$-dT40 condensates (prepared at a [T]/[Arg] ratio of 0.4) showed rapid fusion upon contact. Using our OTF assay, we measured the inverse capillary velocity of these condensates and found it to be ~3.4 $\pm$ 0.2 ms/ μm in a buffer containing 25 mM Tris-HCl, 25 mM NaCl (pH 7.5) (Fig. S2 *A*). We note that passive fusion experiments on a Tween-coated microscope coverslip yielded a characteristic fusion relaxation time that is more than an order of magnitude higher (~100 ms/μm), clearly pointing out the dominant effect of surface drag force on coalescence dynamics of these condensates (Fig. S2 *B*; Videos S1 and S2). Simultaneously, VPT experiments revealed that these [RGRGG]$_5$-dT40 condensates have a viscosity of ~6 $\pm$ 1 Pa·s. We further confirmed that the bead size and concentration had no significant effects on the phase boundaries and the dynamics of these condensates (Fig. S3). Combining the two measurements, we estimate their surface tension to be ~1.6 $\pm$ 0.4 mN/m. Although the viscosity value is qualitatively consistent with previous literature reports on heterotypic condensates formed by disordered protein and RNA mixtures (36), our estimated value of surface tension is higher than previously reported values of the same for

biomolecular condensates (29). One reason for the observed difference could be that we are using salt concentrations that are lower than the physiological salt condition. The observed surface tension value, however, is similar to the previously reported values for complex coacervates (37).

The internal dynamics of protein-NA condensates (i.e., the mobility of individual polypeptide and NA molecules) can be probed using FCS. In contrast to a more traditional approach of fluorescence recovery after photobleaching, which yields diffusivity dynamics that is highly dependent on the choice of model to analyze the experimental data (38), FCS provides a more direct approach (39). Briefly, fluorescence time traces for the fluorescently labeled polypeptide or DNA molecules are recorded from a small confocal volume near the center of the condensates (Fig. 1 *E*). Signal fluctuations due to the diffusion of fluorescent molecules through the confocal volume are analyzed by means of calculating the autocorrelation function (Fig. 1 *F*). The characteristic decay time of the resulting autocorrelation curve provides direct information on their hydrodynamic properties (Fig. 1 *F*). Therefore, the knowledge of the confocal volume size and shape enables the determination of the diffusion coefficient *D* of a given fluorescent species. Because condensates are expected to have a higher

index of refraction than water (as indicated by the feasibility of optical trapping), one key technical consideration is the sensitivity of confocal FCS to the refractive index mismatch between the solution under investigation and the immersion water. Previously, Sherman et al. characterized such an effect and observed that confocal FCS can be reliably used to accurately estimate diffusion coefficients of proteins and small molecules in solutions with refractive indices ranging from 1.33 to 1.46 (40). Consistent with their report, our FCS measurements provided a reliable determination of diffusion coefficients of particles in solvent media with refractive indices ranging from 1.33 to 1.41 (Fig. S4). In brief, we determined the diffusion coefficient of 20-nm fluorescent beads in 0–60% glycerol-water mixtures using FCS and estimated the viscosity of the medium utilizing the Stokes-Einstein relation: $D = k_B T / 6\pi\eta R_h$ (D = diffusion coefficient, k_B = Boltzmann constant, η = viscosity of the medium, R_h = hydrodynamic radius of the probe molecule). Our estimated values of solvent viscosity matched closely with the known values of solvent viscosity for various glycerol-water mixtures (Fig. S4).

Using FCS, we obtained diffusion coefficients of [RGRGG]$_5$ polypeptide and dT40 DNA in the dense phase (condensates prepared at a [T]/[Arg] ratio of 0.4 in a buffer containing 25 mM Tris-HCl, 25 mM NaCl (pH 7.5)), which are ~0.3–0.4 μm^2/s. These values are ~3 orders-of-magnitude lower than those for these molecules in the dilute buffer

solution (Fig. 1 G). Next, to further validate our multiparametric approach, we performed the MSD analysis and droplet fusion experiments using condensates prepared at a fixed [T]/[Arg] ratio of 0.4 with varying NaCl concentrations. In parallel, we determined the diffusion coefficients of RGRGG-repeat polypeptide and dT40 molecules in the dense phase as a function of salt concentration using FCS. Increasing [NaCl] is expected to weaken the ionic attractions between [RGRGG]$_5$ and dT40 chains by decreasing the Debye length (41). Therefore, it is expected that the intermolecular network of these condensates would also weaken with increasing salt if ionic interactions contribute to the stability of these condensates (42). Indeed, we observed that the viscosity of [RGRGG]$_5$-dT40 condensates decreases from ~6 Pa·s at 25 mM NaCl to ~0.89 Pa·s at 425 mM NaCl (Fig. 2 A). Furthermore, our experimental results are consistent with previous reports that predicted a stretched exponential dependence of the viscosity of complex coacervates ($\eta \propto \exp(-\sqrt{C_{salt}})$) on the salt concentration (43,44). The interfacial tension of [RGRGG]$_5$-dT40 condensates also decreases with increasing salt concentration (Fig. 2 B). These findings are in good agreement with previous experimental and theoretical reports on salt-mediated variations of viscosity and interfacial tensions of complex coacervates (37). We observed that the surface tension of peptide-DNA condensates approximately follows a well-known mean-field critical scaling (37): $\gamma \propto (C_{salt} - C_{crit})^{3/2}$
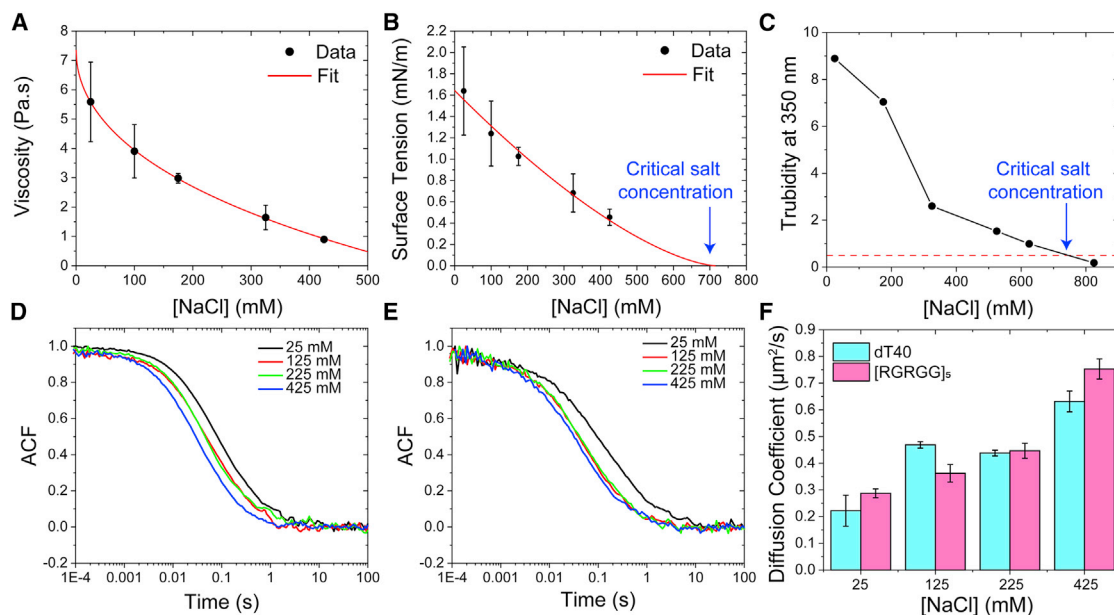
FIGURE 2 Quantification of viscosity, surface tension, and biomolecular diffusion in [RGRGG]$_5$-dT40 condensates. (*A*) Variation of the condensate viscosity as a function of increasing [NaCl] is shown. The black points are the data and the red line is a fit using a stretched exponential function. The corresponding MSD plots are shown in Fig. S6. (*B*) Variation of the condensate surface tension as a function of increasing [NaCl] is shown. The black points are the data and the red line is a fit to a power law with exponent 3/2. The corresponding scaled relaxation times are shown in Fig. S7. The predicted critical value of [NaCl] is shown by a blue arrow. (*C*) Experimental determination of the critical [NaCl] for the same condensates as in (*B*) using the solution turbidity assay is shown. (*D* and *E*) Fluorescence autocorrelation curves are shown for the peptide and ssDNA chains at variable ionic strengths of the buffer, respectively (also see Fig. S5). (*F*) A plot summarizing FCS-derived diffusion coefficients of [RGRGG]$_5$ and dT40 as a function of [NaCl] within the dense phase is given. All error bars represent ± 1 standard deviation.

with an estimated critical salt concentration C_{crit} of 710 $\pm$ 50 mM (Fig. 2 B). To confirm the accuracy of the measured surface tension values, we next measured the turbidity of [RGRGG]$_5$-dT40 mixtures at variable salt concentrations and complemented these measurements with optical microscopy. Indeed, we observed that the phase separation of [RGRGG]$_5$-dT40 mixture vanishes at ~700 mM salt concentration (Figs. 2 C and S1 B), which is consistent with our power law fit to the interfacial tension data. In addition, in qualitative agreement with the VPT-derived viscosity data, we observed that both peptide and single-stranded DNA (ssDNA) diffusion coefficients increase ~3-fold in response to an increase in the salt concentration from 25 mM NaCl to 425 mM NaCl (Fig. 2, D–F). These results suggest that the diffusivity dynamics of component molecules is correlated with the viscosity of the dense phase. This correlation is qualitatively consistent with the Stokes-Einstein relation, which implies that the product $D\eta$ is a constant at a fixed temperature and particle size. However, the peptide and ssDNA molecules are likely to undergo diffusion as complexes and not as free chains in the dense phase. The size distribution of these complexes may be sensitive to the ionic strength of the buffer, which may explain the observed discrepancy in the viscosity scaling with salt from our VPT assay (six-fold change) and the diffusion scaling with salt from the FCS experiments (three-fold change).

Effect of mixture stoichiometry on viscosity, biomolecular diffusion, and surface tension of [RGRGG]$_5$-ssDNA condensates

Reentrant phase transition is a result of a delicate interplay between attractive and repulsive forces that are sensitively dependent on the relative stoichiometry of protein and NA chains (Fig. 3 A; (22,45)). To probe how these multicomponent condensates are impacted by the changes in NA-to-protein mixture stoichiometry, we first measured the diffusivity dynamics of component molecules within the condensate using FCS. Remarkably, we found that the diffusion coefficients of the RGRGG-repeat polypeptide and dT40 DNA remained unaltered as we varied the nucleotide/Arg ratio from 0.08 to 1.6 in the bulk (Fig. 3 B). These data imply that the dynamics of the condensate core is not substantially impacted by the variations in bulk mixture composition. To complement these FCS-based diffusion measurements, we next estimated condensate viscosity using our VPT assay
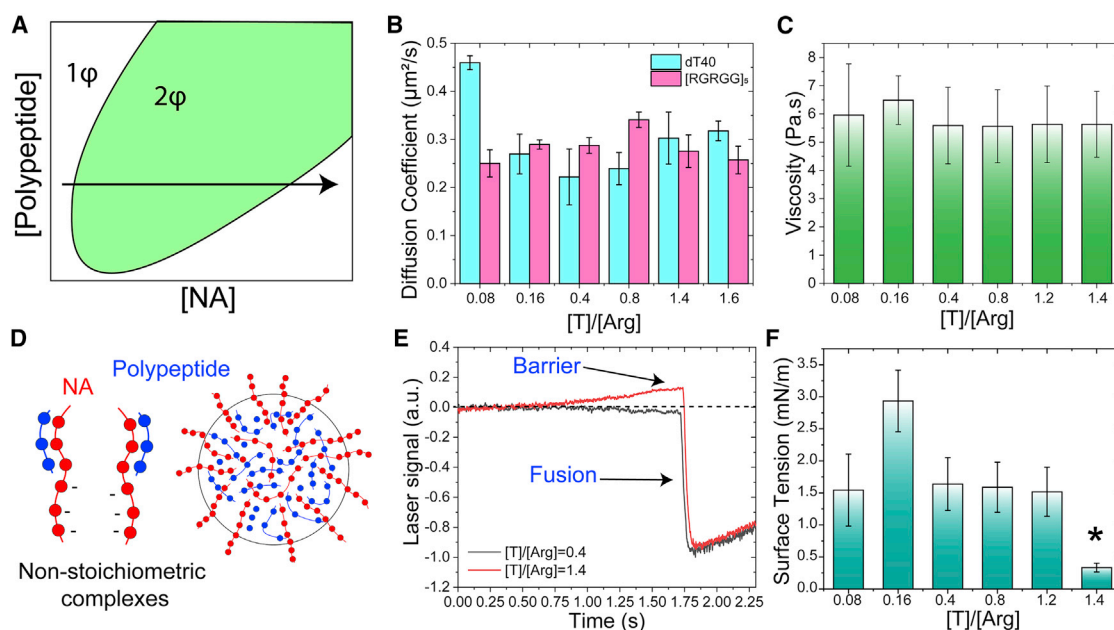
FIGURE 3 The role of mixture composition on the dynamical and surface properties of [RGRGG]$_5$-dT40 condensates. (*A*) Schematic of a reentrant phase diagram shows the formation and dissolution of heterotypic multicomponent condensates as the concentration of one component (nucleic acid) is continuously varied (*horizontal black arrow*), whereas the concentration of the other component (polypeptide) stays constant. (*B*) A plot summarizing FCS-derived diffusion coefficients of [RGRGG]$_5$ and dT40 in the dense phase as a function of DNA/peptide ratio. The corresponding autocorrelation plots are shown in Fig. S8. (*C*) Variation in condensate viscosity as a function of DNA/peptide ratio is shown. The corresponding MSD plots are shown in Fig. S9. (*D*) A schematic depiction is shown of nonstoichiometric partially charged peptide-NA complexes and their condensates with the surface decorated by the partially-complexed charged species. (*E*) Evidence of a kinetic barrier in the force relaxation curve (*red*) from the condensate fusion experiments for condensates formed at excess dT40 conditions (also see Video S4) is shown. Such a kinetic barrier was absent for nearly charged-matched condensates (*black curve*). (*F*) Variation of condensate surface tension as a function of DNA/peptide ratio is shown. The corresponding scaled relaxation times are shown in Fig. S10. The asterisk for the sample prepared at [T]/[Arg] ratio of 1.4 indicates the existence of a kinetic barrier of droplet coalescence. All error bars represent $\pm$ 1 standard deviation.

and observed an almost constant value within the same window of mixture composition (Fig. 3 C). Combining these two results, we observed that the product $D\eta$ stays almost unchanged across this entire range of mixing ratios. Considering that we have varied the mixture composition over more than one order of magnitude, our viscosity and diffusion measurements suggest that the core dynamics of [RGRGG]$_5$-ssDNA condensates is insensitive to variation in mixture composition.

How do the surface properties of polypeptide-NA condensates vary with bulk mixture composition? Previously, we have shown that at mixture compositions far from the charged-matched stoichiometric conditions, partially condensed "tadpole-like" complexes are formed (23). These partially screened complexes are expected to have larger solvation volume and may prefer to occupy the surface of the condensates, where solvent exposure is warranted (Fig. 3 D; (46)). This phenomenon is expected to lower the interfacial tension of the condensate because of a surfactant-like action of the partially-screened tadpole-like complexes (Fig. 3 D). This model of reentrant condensation, originally proposed by Shklovskii and Zhang (47), therefore suggests that the condensates' surface architecture is sensitively dependent on the mixture stoichiometry. Indeed, electrophoretic light scattering measurements previously revealed that these heterotypic condensates undergo a charge inversion as the NA/protein ratio increases in the bulk (22). These observations led us to hypothesize that the colloidal stability of the dispersed protein-NA droplets against coalescence increases far from stoichiometric conditions. To test this idea, we measured the surface tension of [RGRGG]$_5$-dT40 condensates at nucleotide/Arg ratios ranging from 0.08 to 1.4. We observed that unlike condensates formed at a low NA/protein ratio, condensates with excess dT40 ([T]:[Arg] = 1.4) resisted coalescence (Fig. 3 E) and showed a clear barrier in the laser signal preceding their coalescence, which is indicative of a repulsive force (48). These data are consistent with the aforementioned argument that the surfaces of protein-NA condensates are altered with mixture composition and that the surface tension is substantially lowered for condensates prepared at excess NA. Indeed, we observed that these condensates have ∼4-fold-lower interfacial tension as compared with condensates formed at ([T]:[Arg] = 0.4, Fig. 3 F). The observed barrier in the force relaxation curve during droplet coalescence at the single condensate level indicates that the condensate surface carries a net negative charge, which is consistent with the previously reported ensemble electrophoretic mobility measurements of peptide-RNA condensates prepared at a high RNA concentration (22). Additionally, increasing the nucleotide/Arg ratio to 1.6 ([T]:[Arg] = 1.6) resulted in condensates that did not undergo fusion, even under our optical traps (Video S3; also see Video S4).

Because the polypeptide/DNA diffusion coefficient at the core of these condensates and the measured viscosity values remain unaltered for condensates prepared at an NA/peptide ratio of 1.4 as compared with the condensates formed at lower ssDNA, we conclude that the observed kinetic barrier in droplet coalescence at a relatively high NA concentration is not due to the increased viscosity but due to the decreased surface tension of [RGRGG]$_5$-dT40 condensates (Fig. 3, E and F; Videos S3 and S4). Taken together, our results suggest that a reentrant transition accompanies a nonmonotonic variation in the surface architecture of protein-NA condensates without being accompanied by drastic changes in the dynamical properties of the condensate core.

Conclusions

RNP LLPS in cell cytoplasm/nucleoplasm sensitively depends on the RNA/RNP ratio, giving rise to a rich nonmonotonic phase behavior that is best understood using the framework of reentrant phase transition (20,45) and is marked by a phase separation event at low RNA-to-RNP stoichiometry and the emergence of a homogenous single-phase at a high RNA/RNP ratio. The data reported here suggest that the composition of multicomponent heterotypic condensates plays a fundamental role not only in the formation and dissolution of these condensates but also in controlling their mesoscale structure. By quantifying the viscosity and surface tension of peptide-NA condensates, we find that the surfaces of these condensates are dependent on the bulk mixture composition, whereas the dynamical properties of the condensate core remain relatively independent thereof. The tunability in the surface properties of multicomponent heterotypic condensates provide a potential regulatory mechanism of condensate interactions with their surroundings and with each other in the subcellular space.

To construct a thermodynamic basis for our observation, we computed a phase diagram along with the equilibrium tie lines (that connect the dilute phase composition with that of the dense phase) for a multicomponent mixture with the use of a Flory-Huggins-type model (see Supporting materials and methods for further details) (24,45). From this model phase diagram (Fig. 4 A), which reveals a closed loop with two critical points, we see that as we increase the component 2 concentration at a fixed concentration of component 1, the total polymer concentrations in the dense phase do not change significantly if the upper end of the tie line closely follows a constant volume fraction line (Fig. 4 A). In such a case, the density and hence the viscosity of the condensates is expected to be insensitive to the variation in the bulk mixture composition. Therefore, our observation that the viscosity of the dense phase remains unaltered at varied mixture compositions is likely a manifestation of a near-constant total concentration of the peptide and ssDNA in the dense phase (Fig. 4 A), which is ultimately governed by the orientation of the equilibrium tie lines and regulated by the relative magnitudes of respective homotypic and heterotypic interactions in a multicomponent
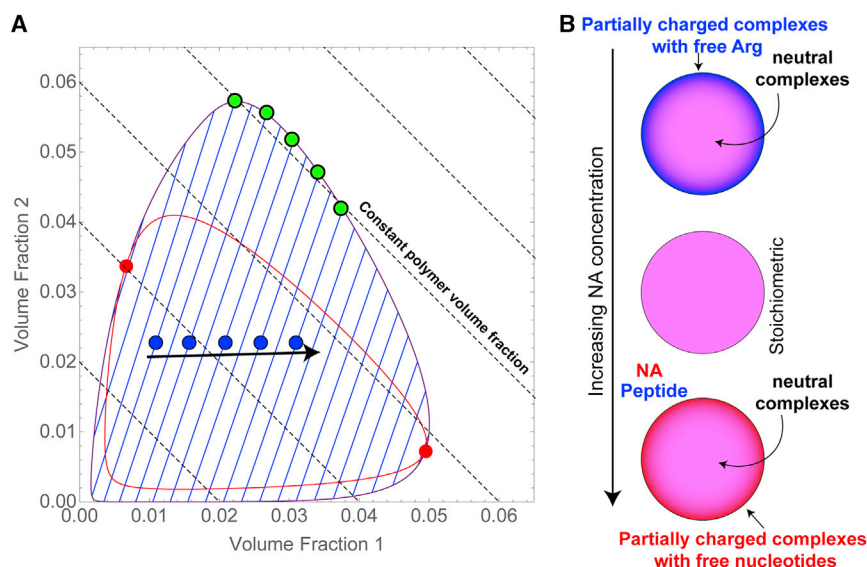
FIGURE 4 Proposed model of multicomponent phase separation and the formation of spatially organized condensates. (*A*) A closed-loop phase diagram computed using a Flory-Huggins-type free energy model, as described in the Supporting materials and methods. Spinodal curve and critical points are red, coexistence curve is purple and tie lines are blue. Dashed lines show constant solute volume fractions. The solid arrow indicates increasing the volume fraction of one component in the bulk while keeping the other component fixed (*blue circles* represent the bulk concentration of components). This results in changes in total polymer volume fraction in the dense phase in a very narrow range (*green circles*), as governed by the orientation of the tie lines. (*B*) A scheme showing that the surface of heterotypic protein-nucleic acid condensates is sensitively dependent on the bulk mixture composition, giving rise to tunable spatially-organized condensates that have low interfacial tensions at nonstoichiometric mixture compositions.

mixture (Fig. S13). We note that, although the scaling of viscosity with polymer volume fraction is still a subject of research in polymer dynamics, the proposition that variable volume fraction implies variable viscosity is well established (25). Surface tension, on the other hand, is determined by the proximity of the system to the nearest of the two critical points and also by the surface charge of the peptide-NA condensates. The accumulation of partially-charged complexes on the condensate surface becomes more significant as one moves further from the stoichiometric mixture composition (23). This scenario leads to the spatially organized core-shell structure of multicomponent protein-NA condensates that phase separate via heterotypic interactions (Fig. 4 *B*). Future studies can refine this thermodynamic model by measuring and modeling homotypic and heterotypic interactions in a multicomponent mixture. Finally, the application of frequency-dependent rheological measurements (42,49) will be valuable for probing the network structure of multicomponent biomolecular condensates and quantifying their viscous and elastic responses as a function of polypeptide/NA sequence composition and patterning. Such studies are currently underway.

SUPPORTING MATERIAL

Supporting Material can be found online at https://doi.org/10.1016/j.bpj.2021.01.005.

AUTHOR CONTRIBUTIONS

P.R.B. and I.A. conceived the idea and designed the experiments. I.A. performed the experiments and analyzed the data with help from P.R.B. G.M.T. performed the numerical simulations and calculated the theoretical phase diagram. All authors contributed to writing the manuscript.

ACKNOWLEDGMENTS

SUPPORTING CITATIONS

References (50–64) appear in the Supporting materials and methods.

REFERENCES

1. Banani, S. F., H. O. Lee, …, M. K. Rosen. 2017. Biomolecular condensates: organizers of cellular biochemistry. *Nat. Rev. Mol. Cell Biol.* 18:285–298.

2. Shin, Y., and C. P. Brangwynne. 2017. Liquid phase condensation in cell physiology and disease. *Science.* 357:eaaf4382.

3. Mitrea, D. M., and R. W. Kriwacki. 2016. Phase separation in biology; functional organization of a higher order. *Cell Commun. Signal.* 14:1.

4. Lyon, A. S., W. B. Peeples, and M. K. Rosen. 2020. A framework for understanding the functions of biomolecular condensates across scales. *Nat. Rev. Mol. Cell Biol.* Published online Novemeber 9, 2020. https://doi.org/10.1038/s41580-020-00303-z.

5. Ladouceur, A.-M., B. S. Parmar, …, S. C. Weber. 2020. Clusters of bacterial RNA polymerase are biomolecular condensates that assemble through liquid-liquid phase separation. *Proc. Natl. Acad. Sci. USA.* 117:18540–18549.

6. Guilhas, B., J.-C. Walter, …, M. Nollmann. 2020. ATP-driven separation of liquid phase condensates in bacteria. *Mol. Cell.* 79:293–303.e4.

7. Cohan, M. C., and R. V. Pappu. 2020. Making the case for disordered proteins and biomolecular condensates in bacteria. *Trends Biochem. Sci.* 45:668–680.

8. Alberti, S. 2017. Phase separation in biology. *Curr. Biol.* 27:R1097–R1102.

9. Forman-Kay, J. D., R. W. Kriwacki, and G. Seydoux. 2018. Phase separation in biology and disease. *J. Mol. Biol.* 430:4603–4606.

10. Hyman, A. A., C. A. Weber, and F. Jülicher. 2014. Liquid-liquid phase separation in biology. *Annu. Rev. Cell Dev. Biol.* 30:39–58.

11. Nedelsky, N. B., and J. P. Taylor. 2019. Bridging biophysics and neurology: aberrant phase transitions in neurodegenerative disease. *Nat. Rev. Neurol.* 15:272–286.

12. Lee, K. H., P. Zhang, …, J. P. Taylor. 2016. C9orf72 dipeptide repeats impair the assembly, dynamics, and function of membrane-less organelles. *Cell.* 167:774–788.e17.

13. Basu, S., S. D. Mackowiak, …, D. Hnisz. 2020. Unblending of transcriptional condensates in human repeat expansion disease. *Cell.* 181:1062–1079.e30.

14. Mathieu, C., R. V. Pappu, and J. P. Taylor. 2020. Beyond aggregation: pathological phase transitions in neurodegenerative disease. *Science.* 370:56–60.

15. Roden, C., and A. S. Gladfelter. 2020. RNA contributions to the form and function of biomolecular condensates. *Nat. Rev. Mol. Cell Biol* Published online July 6, 2020. https://doi.org/10.1038/s41580-020-0264-6.

16. Schwartz, J. C., X. Wang, …, T. R. Cech. 2013. RNA seeds higher-order assembly of FUS protein. *Cell Rep.* 5:918–925.

17. Harami, G. M., Z. J. Kovács, …, M. Kovács. 2020. Phase separation by ssDNA binding protein controlled via protein-protein and protein-DNA interactions. *Proc. Natl. Acad. Sci. USA.* 117:26206–26217.

18. Yamazaki, T., S. Souquere, …, T. Hirose. 2018. Functional domains of NEAT1 architectural lncRNA induce paraspeckle assembly through phase separation. *Mol. Cell.* 70:1038–1053.e7.

19. Guillén-Boixet, J., A. Kopach, …, D. Mateju. 2020. RNA-induced conformational switching and clustering of G3BP drive stress granule assembly by condensation. *Cell.* 181:346–361.e17.

20. Banerjee, P. R., A. N. Milin, …, A. A. Deniz. 2017. Reentrant phase transition drives dynamic substructure formation in ribonucleoprotein droplets. *Angew. Chem. Int.Engl.* 56:11354–11359.

21. Maharana, S., J. Wang, …, S. Alberti. 2018. RNA buffers the phase separation behavior of prion-like RNA binding proteins. *Science.* 360:918–921.

22. Alshareedah, I., T. Kaur, …, P. R. Banerjee. 2019. Interplay between short-range attraction and long-range repulsion controls reentrant liquid condensation of ribonucleoprotein-RNA complexes. *J. Am. Chem. Soc.* 141:14593–14602.

23. Alshareedah, I., M. M. Moosa, …, P. R. Banerjee. 2020. Phase transition of RNA-protein complexes into ordered hollow condensates. *Proc. Natl. Acad. Sci. USA.* 117:15650–15658.

24. Riback, J. A., L. Zhu, …, C. P. Brangwynne. 2020. Composition-dependent thermodynamics of intracellular phase separation. *Nature.* 581:209–214.

25. Rubinstein, M., and R. H. Colby. 2003. Unentangled Polymer Dynamics and Entangled Polymer Dymanics. Polymer Physics. Oxford University Press, New York, p. 309, 361.

26. Kaur, T., I. Alshareedah, …, P. R. Banerjee. 2019. Molecular crowding tunes material states of ribonucleoprotein condensates. *Biomolecules.* 9:71.

27. Patel, A., H. O. Lee, …, S. Alberti. 2015. A liquid-to-solid phase transition of the ALS protein FUS accelerated by disease mutation. *Cell.* 162:1066–1077.

28. Ghosh, A., and H.-X. Zhou. 2020. Determinants for fusion speed of biomolecular droplets. *Angew. Chem. Int.Engl.* 59:20837–20840.

29. Jeon, B. J., D. T. Nguyen, …, O. A. Saleh. 2018. Salt-dependent properties of a coacervate-like, self-assembled DNA liquid. *Soft Matter.* 14:7009–7015.

30. Alshareedah, I., T. Kaur, and P. R. Banerjee. 2020. Methods for characterizing the material properties of biomolecular condensates. Methods in Enzymology646. Academic Press, pp. 143–183.

31. Fisher, R. S., and S. Elbaum-Garfinkle. 2020. Tunable multiphase dynamics of arginine and lysine liquid condensates. *Nat. Commun.* 11:4628.

32. Nguyen, D. T., B. J. Jeon, …, O. A. Saleh. 2019. Length-dependence and spatial structure of DNA partitioning into a DNA liquid. *Langmuir.* 35:14849–14854.

33. Blocher, W. C., and S. L. Perry. 2017. Complex coacervate-based materials for biomedicine. *Wiley Interdiscip. Rev. Nanomed. Nanobiotechnol.* 9:e1442.

34. Lund, M., and B. Jönsson. 2013. Charge regulation in biomolecular solution. *Q. Rev. Biophys.* 46:265–281.

35. Wahle, C. W., K. M. Martini, …, G. M. Thurston. 2017. Model for screened, charge-regulated electrostatics of an eye lens protein: bovine gammaB-crystallin. *Phys. Rev. E.* 96:032415.

36. Elbaum-Garfinkle, S., Y. Kim, …, C. P. Brangwynne. 2015. The disordered P granule protein LAF-1 drives phase separation into droplets with tunable viscosity and dynamics. *Proc. Natl. Acad. Sci. USA.* 112:7189–7194.

37. Spruijt, E., J. Sprakel, …, J. van der Gucht. 2010. Interfacial tension between a complex coacervate phase and its coexisting aqueous phase. *Soft Matter.* 6:172–178.

38. Taylor, N. O., M. T. Wei, …, C. P. Brangwynne. 2019. Quantifying dynamics in phase-separated condensates using fluorescence recovery after photobleaching. *Biophys. J.* 117:1285–1300.

39. Wei, M. T., S. Elbaum-Garfinkle, …, C. P. Brangwynne. 2017. Phase behaviour of disordered proteins underlying low density and high permeability of liquid organelles. *Nat. Chem.* 9:1118–1125.

40. Sherman, E., A. Itkin, …, G. Haran. 2008. Using fluorescence correlation spectroscopy to study conformational changes in denatured proteins. *Biophys. J.* 94:4819–4827.

41. Onuchic, P. L., A. N. Milin, …, P. R. Banerjee. 2019. Divalent cations can control a switch-like behavior in heterotypic and homotypic RNA coacervates. *Sci. Rep.* 9:12161.

42. Jawerth, L. M., M. Ijavi, …, E. Fischer-Friedrich. 2018. Salt-dependent rheology and surface tension of protein condensates using optical traps. *Phys. Rev. Lett.* 121:258101.

43. Rubinstein, M., and A. N. Semenov. 2001. Dynamics of entangled solutions of associating polymers. *Macromolecules.* 34:1058–1068.

44. Spruijt, E., M. A. Cohen Stuart, and J. van der Gucht. 2013. Linear viscoelasticity of polyelectrolyte complex coacervates. *Macromolecules.* 46:1633–1641.

45. Choi, J. M., F. Dar, and R. V. Pappu. 2019. LASSI: a lattice model for simulating phase transitions of multivalent proteins. *PLoS Comput. Biol.* 15:e1007028.

46. Harmon, T. S., A. S. Holehouse, and R. V. Pappu. 2018. Differential solvation of intrinsically disordered linkers drives the formation of spatially organized droplets in ternary systems of linear multivalent proteins. *New J. Phys.* 20:045002.

47. Zhang, R., and B. I. Shklovskii. 2005. Phase diagram of solution of oppositely charged polyelectrolytes. *Physica A.* 352:216–238.

48. Welsh, T. J., G. Krainer, …, T. P. J. Knowles. 2020. Surface electrostatics govern the emulsion stability of biomolecular condensates. *bioRxiv* https://doi.org/10.1101/2020.04.20.047910.

49. Jawerth, L., E. Fischer-Friedrich, …, F. Jülicher. 2020. Protein condensates as aging Maxwell fluids. *Science.* 370:1317–1323.

50. Banerjee, P. R., D. M. Mitrea, …, A. A. Deniz. 2016. Asymmetric modulation of protein order-disorder transitions by phosphorylation and partner binding. *Angew. Chem. Int.Engl.* 55:1675–1679.

51. McGlynn, J. A., N. Wu, and K. M. Schultz. 2020. Multiple particle tracking microrheological characterization: fundamentals, emerging techniques and applications. *J. Appl. Phys.* 127:201101.

52. Tinevez, J.-Y., N. Perry, …, K. W. Eliceiri. 2017. TrackMate: an open and extensible platform for single-particle tracking. *Methods.* 115:80–90.

53. Allan, D., C. van der Wel, …, A. Ahmadia. 2019. soft-matter/trackpy: Trackpy v0.4.2 https://zenodo.org/record/3492186.

54. Muller, P. 2012. A multiple-tau algorithm for Python/NumPymultiple-tau algorithm (Version 0.1.9). Available at Accessed 15 Sep 2020 https://pypi.python.org/pypi/multipletau/.

55. Enderlein, J., I. Gregor, …, U. B. Kaupp. 2005. Performance of fluorescence correlation spectroscopy for measuring diffusion and concentration. *ChemPhysChem.* 6:2324–2336.

56. Rüttinger, S., V. Buschmann, …, F. Koberling. 2008. Comparison and accuracy of methods to determine the confocal volume for quantitative fluorescence correlation spectroscopy. *J. Microsc.* 232:343–352.

57. Schindelin, J., I. Arganda-Carreras, …, A. Cardona. 2012. Fiji: an open-source platform for biological-image analysis. *Nat. Methods.* 9:676–682.

58. Dobkin, D. P., A. R. Wilks, …, W. P. Thurston. 1990. Contour tracing by piecewise linear approximations. *ACM Trans. Graph.* 9:389–423.

59. Cheng, N.-S. 2008. Formula for the viscosity of a glycerol− water mixture. *Ind. Eng. Chem. Res.* 47:3285–3288.

60. Volk, A., and C. J. Kähler. 2018. Density model for aqueous glycerol solutions. *Exp. Fluids.* 59:75.

61. Segur, J. B., and H. E. Oberstar. 1951. Viscosity of glycerol and its aqueous solutions. *Ind. Eng. Chem.* 43:2117–2120.

62. Widengren, J., U. Mets, and R. Rigler. 1995. Fluorescence correlation spectroscopy of triplet states in solution: a theoretical and experimental study. *J. Phys. Chem.* 99:13368–13379.

63. Banerjee, P. R., M. M. Moosa, and A. A. Deniz. 2016. Two-dimensional crowding uncovers a hidden conformation of α-Synuclein. *Angew. Chem. Int.Engl.* 55:12789–12792.

64. Banerjee, P. R., and A. A. Deniz. 2014. Shedding light on protein folding landscapes by single-molecule fluorescence. *Chem. Soc. Rev.* 43:1172–1188.

Supplemental information

Quantifying viscosity and surface tension of multicomponent protein-nucleic acid condensates

Ibraheem Alshareedah, George M. Thurston, and Priya R. Banerjee

Materials and Methods

Peptide and DNA sample preparation: The peptide ([RGRGG]$_5$) was purchased from Genscript USA Inc. (NJ, USA) and contains a C-terminal cysteine for site-specific peptide labeling. Peptide stock solutions were prepared in RNase-free water (Santa Cruz Biotechnology) with 50 mM dithiothreitol (DTT). Custom-synthesized DNA oligos, poly(dT)-T40 [40 nucleobases; molecular weight =12106 Da] and Atto488 labeled (5')-dT40 were purchased from Integrated DNA Technologies (IDT). The DNAs were reconstituted in RNase-free water. The concentration of DNA stocks was calculated from their respective measured absorbance at 260 nm in a UV-Vis spectrophotometer (Nanodrop oneC). Both DNA and peptide stock solutions were stored at −20 °C. All peptide-DNA condensates were prepared in a buffer containing 25 mM Tris-HCl (pH 7.5), 25 mM NaCl and 20 mM DTT unless otherwise noted. The peptide concentration was kept at 5.0 mg/ml (~2 mM) throughout this study and the DNA concentration was varied as indicated.

All concentrations in this paper are reported in [nucleotide]:[Arg] molar ratios.

Fluorescence labeling: The RGRGG repeat peptide contains a C-terminal cysteine which was used for site-specific labeling with Alexa594 dyes using the same protocol (Cys-maleimide chemistry) as described in our earlier work[1-5]. The labeling efficiency for the peptide samples was observed to be ≥ 90% (UV-Vis absorption measurements).

Fusion of suspended droplets using optical traps: Optical trap mediated droplet fusion assays were conducted to investigate the inverse capillary velocity of DNA-peptide condensates, as previously described[6]. Briefly, samples containing DNA-peptide condensates at the indicated [T]/[Arg] ratios were injected into a tween 20-coated (20% v/v) 25 mm x 75 mm x 0.1 mm flow chamber (custom-made). Condensates were trapped using a dual-trap optical tweezer system that also offers laser scanning confocal fluorescence microscopy (LUMICKS™, C-trap). Droplets were independently trapped far from each other in two optical traps (using a 1064 nm laser) and then brought into proximity. The 2nd trap was held at a fixed position while the 1st trap was programmed to move at a constant speed of 40-100 nm/s in the direction of the 2nd trap. Coalescence started upon contact due to interfacial tension. The motion of the 1st trap was stopped when the fused droplet relaxed to a spherical shape. The force-time signal was recorded at a 78.2 kHz sampling frequency (i.e., ~13 μs time interval) and analyzed using the following fusion relaxation model[7]:

$$F = ae^{(-t/\tau)} + bt + c \qquad (1)$$

where the parameter τ is the fusion relaxation time. The 2nd term in equation (1) accounts for the constant velocity of the 1st trap. ~ 10-20 fusion events were recorded for each sample, then and the corresponding relaxation time was plotted as a function of the average diameter (as determined by fluorescence images before fusion) of the fusing droplets and fitted using a linear model of inverse capillary velocity[8].

Video Particle Tracking (VPT) Microscopy: Samples were prepared by mixing the polypeptide and the ssDNA in a buffer containing fluorescent beads (0.0003% solids, 200 nm carboxylate-coated yellow-green polystyrene spheres; FluoSpheres™, Invitrogen). Upon condensate formation, beads were found to be embedded in the condensates (see Fig. 1c, main text). Next, samples were placed on a tween 20-coated (20% v/v) microscope coverslip and sandwiched with a 1 mm thick microscope glass slide as described in our earlier work[8]. Following that, oil was injected into the chamber to prevent evaporation-induced hydrodynamic currents within the sample. After sealing with oil, samples were left to equilibrate for 0.5-2 hours or until all droplets have settled on the glass surface. Samples were then imaged using an epifluorescence microscope (Zeiss Primovert inverted iLED microscope with a 100× oil-immersion objective lens

and a Zeiss Axiocam 503 monochrome camera). Movies capturing the Brownian motion of the fluorescent beads within peptide-DNA condensates were collected at variable acquisition rates to ensure that the measured viscosity is independent of the acquisition rate of the microscope[9]. For each peptide-DNA mixing ratio, three independent samples were made on different days, 2-4 movies/per sample were collected imaging a total of 5-10 condensates, each condensate contained 10-100 microspheres. Particle tracking was done using the open-source particle tracking software TrackMate[10] (v6.0.1). Tracking results were also cross-validated using TrackPy python-based particle tracking library (v0.4.2)[11]. Trajectories were corrected for sample-stage drift and then the mean squared displacement (MSD) was calculated for each trajectory using a custom-built python script as a function of the lag time (τ). To eliminate any effects coming from the interface of the condensate with the surrounding dilute phase, trajectories of particles that are proximal to the interface were discarded. The ensemble-averaged MSD was obtained and fitted using the following equation

$$MSD(\tau) = <r^2>(\tau) = 4D\tau^\alpha \qquad (2)$$

Where D is the diffusion coefficient of the bead and α is the diffusive exponent. For classical Brownian motion in a purely viscous fluid, the value of α is equal to unity. α values for all the condensates tested were in the range of 0.9-1.2. The viscosity η of the condensate is then determined using the Stokes-Einstein equation ($\eta = \frac{k_B T}{6\pi DR}$), where D = diffusion coefficient, k_B = Boltzmann constant, η = viscosity of the medium, R is the radius of the bead, T is the temperature.

Partition coefficient measurements: Images for partition analysis were collected using a Zeiss LSM710 laser scanning confocal microscope with a 63x oil-immersion objective (Plan-Apochromat 63x/1.4 oil DIC M27). The same samples were used for DNA-peptide mixtures as described in the droplet fusion section. All the confocal images were collected within 30 minutes of sample preparation. The partition coefficient (k) was calculated by dividing the mean intensity of Atto488-labeled dT40 or Alexa494-labeled RGRGG repeat polypeptide per unit area inside the droplet by the mean intensity per unit area in the external dilute phase ($k = \frac{I_{in}}{I_{out}}$). For each sample, 30-40 droplets were analyzed.

Turbidity measurements: [RGRGG]$_5$ and dT$_{40}$ mixtures were prepared at a fixed peptide concentration (5 mg/ml) and variable ssDNA concentrations. Sample absorbance at 350 nm was measured using a spectrophotometer (Nanodrop oneC UV-Vis) with an optical path length of 1 mm. Each sample was prepared independently and measured. A similar protocol was followed for recording turbidity of DNA-peptide mixtures at a fixed concentration and composition with variable [NaCl]. For each data point, two independently prepared samples were measured twice.

Fluorescence correlation spectroscopy: Samples containing 10-100 pM bulk concentration of either Atto488-labeled dT40 or Alexa594-labeled [RGRGG]$_5$ were injected into a tween 20-coated 25 mm x 75 mm x 0.1 mm custom-made flow chamber and loaded onto the microscope stage (Lumicks, C-trap) equipped with a single-photon avalanche photodiode (sAPD). We varied the labeled species concentrations such that their concentrations within the condensates are suitable for FCS measurements, which was judged by the signal to noise ratio of the autocorrelation curves. The optimal location for collecting FCS intensity-time traces was selected by first collecting a point Z-scan at the center of the condensate. The location with maximal intensity was identified and measurements of the photon arrival times were acquired at a 72.8 kHz sampling rate by performing a point scan at the center of the peptide-DNA condensate at the optimal location (**Fig. S10**). The excitation power was kept at a minimum to avoid photobleaching of the fluorophores. Each point scan was collected over 5 minutes. For each sample, five point-scans from different condensates were obtained and analyzed as follows. For each point scan, the

autocorrelation function was calculated for different lag times using the multipletau (v0.1.9) and pycorrelate (v0.2.1) python libraries[12,13]. The Autocorrelation function was fitted with the following equation

$$G(\tau) = G_0 \left(1 + \frac{4D\tau}{\omega^2}\right)^{-1} \left(1 + \frac{4D\tau}{\omega_z^2}\right)^{-\frac{1}{2}} + G_{inf} \tag{3}$$

here, D is the diffusion coefficient of the fluorescent probe and ω, ω_z are the radial and axial dimensions of the confocal volume, respectively, under the three-dimensional Gaussian approximation[14]. In the fitting process, the structural parameters ω and ω_z were fixed to the values obtained from the calibration procedure described below and only G_0, D and G_{inf} were allowed to vary. The diffusion coefficient was extracted from the fit for each autocorrelation curve. The diffusion coefficient values were averaged and their standard deviation was taken as the uncertainty. A similar procedure was used for measuring the diffusion of 20 nm beads in glycerol/water mixtures except that the FCS intensity-time traces were collected from random points on the XY plane that is approximately at the middle between the lower and upper surfaces of the sample chamber (about 40 μm above the lower glass surface).

For calibration, we used a combination of free dye molecules as well as fluorescent beads. Briefly, we used Alexa488 dye and Alexa594 to calibrate the lasers by collecting FCS intensity-time series and calculating autocorrelation curves (**Fig. S11**). Then, by fixing the diffusion coefficient D to the known diffusion coefficients of the probes, we performed the fittings to determine the structural parameters of the confocal volume. We also confirmed confocal volume measurements by performing FCS calibration on 20 nm and 200 nm polystyrene beads (FluoSpheres[TM], Invitrogen) in water and found that the confocal volume structural parameters lie within the acceptable range (producing D values of 22.4 μm^2/s and 0.8 μm^2/s, respectively). The diffusion coefficient values for these two bead types in water at 24 °C (the temperature of our microscope chamber) as calculated from the Stokes-Einstein equation are 24.45 and 2.445 μm^2/s, respectively. The value for the 20 nm beads was closer to the accepted values and therefore, 20 nm beads were used to estimate the viscosity of glycerol-water mixtures. The combined calibration procedures yielded a beam waist of 320 ± 20 nm for the green laser line and 340± 20 nm for the red laser line. The beam axial dimension was fluctuating between 2-10 μm. We note that the diffusion-based calibration is not accurate for determining the axial dimension of the confocal volume due to the sensitivity of the correlation plateau to the probe concentration[15]. Nevertheless, the axial dimension is unlikely to contribute to the extracted values of the diffusion coefficient and does not alter the shape of the autocorrelation function[15].

Data processing software: Excel 2016 was used for partition calculations. All numerical/statistical analysis was done in custom-built Python procedures. Fiji-ImageJ[16] (version 1.52p) was used for image processing. OriginPro (2018b) was used for Graphing. Adobe Illustrator CC (2019) was used for the figure assembly and production.

Theoretical Phase Diagram: The liquid-liquid phase separation spinodal, tie lines, and critical points were computed with the use of a Flory-Huggins mixture model with two polymers in a solvent.

$$\frac{F}{k_B T} = \frac{\varphi_1 \ln(\varphi_1)}{\gamma_1} + \frac{\varphi_2 \ln(\varphi_2)}{\gamma_2} + w_{11}\varphi_1^2 + w_{12}\varphi_1\varphi_2 + w_{22}\varphi_2^2 + (\varphi_1 + \varphi_2) + (1 - \varphi_1 - \varphi_2)\ln(1 - \varphi_1 - \varphi_2)$$

Here, the ϕ's are volume fractions, the γ's are size parameters, and the w's are mean-field interaction parameters. The parameters used for the computation of the representative closed-loop boundary were γ_1 = 300, γ_2 = 7000, w_{11} = 1.0, w_{22} = -0.35, and w_{12} = -2.15.

The computation of the closed-loop phase boundaries, spinodal, and critical points, coded in Mathematica, first searches along rays in composition space through the origin, for points at which the least eigenvalue of the Hessian matrix of the free energy taken with respect to the two volume fractions first changes sign from positive to negative. Then, by making small steps in directions orthogonal to the composition-gradient of the determinant of the Hessian, while at the same time correcting periodically to ensure that the full determinant of the Hessian remains zero, a closely spaced series of points is generated along the spinodal. To locate the critical points while stepping along the spinodal, the algorithm also searches for and refines any points on the spinodal at which the directional derivative of the spinodal curve becomes parallel to that eigenvector of the Hessian that belongs to its least eigenvalue.

The method used here for computing the tie lines takes advantage of the fact that the collection of tie lines corresponds to the self-intersections of the mapping of the composition triangle into the space of the three chemical potentials. The mapping is that created by the ternary free energy of mixing, a model in the present case. Because linear terms in the free energy of mixing do not influence the thermodynamic conditions for liquid-liquid phase separation, for numerical work it can be convenient to remove them in advance, as was done for the expression given above, in view of the Taylor expansion of the logarithmic term.

Starting tie lines were located by first identifying a composition point entirely inside the spinodal, evaluating the difference between the chemical potentials of the two solute components at that point, then creating a curve in composition space for which this difference remained the same. The algorithm then maps small segments along this curve into the space of the chemical potentials of the solvent and of component 1, and searches for intersections of the images of those segments in that chemical potential space. Approximate intersections so found are then refined to provide good starting tie lines, by demanding that each chemical potential is the same at each composition endpoint. For numerical work, it was found sometimes helpful to use the logarithms of the volume fractions, due to the low volume fractions that can occur along the coexistence curve.

Finally, having located such a starting, refined tie line, the algorithm makes small steps that remain close to the self-intersections of the chemical potential mapping, then refines each step to continue to require equality of all three chemical potentials. In order to make the small steps in good directions, it is helpful to recognize that directions that will locally follow a collection of tie lines can be written as a generalized cross product of the gradient vectors of each chemical potential, each such vector being a function of the four coordinates that combine the compositions of the two endpoints. An analogous method can be used for following the contours of any differentiable map from R^n to R^{n-1}, closely related to more general methods[17] that inspired the present one[18].
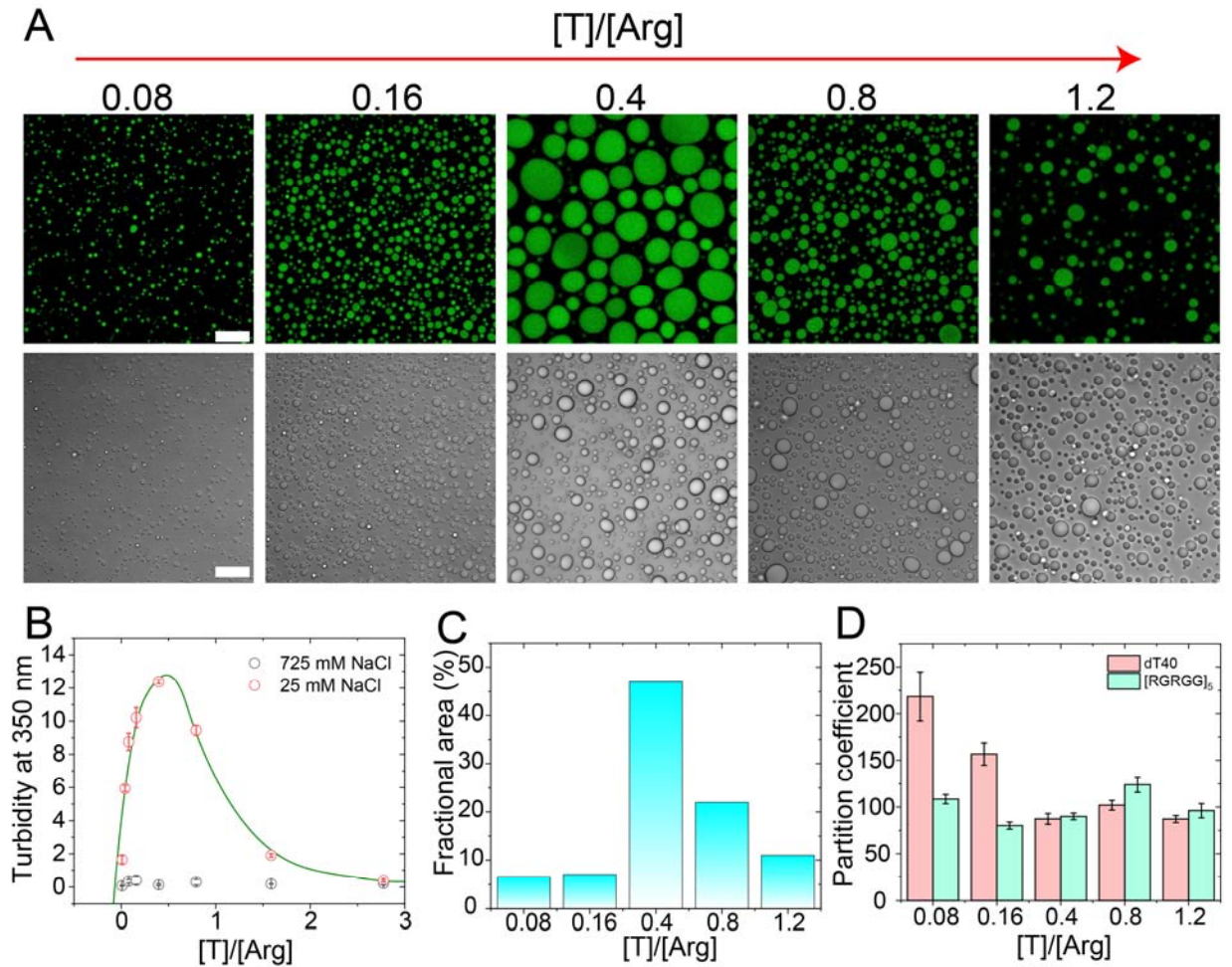
Fig. S1. Condensation of [RGRGG]₅-dT40 mixtures at different [T]/[Arg] ratios. (A) Fluorescence and bright-field images of [RGRGG]₅-dT40 condensates. Scale bars represent 20 µm. **(B)** Turbidity at 350 nm as a function of increasing [T]/[Arg] ratio at 25 mM and 725 mM salt concentrations. The green line is drawn as a guide to the eye. The incubation time for this measurement is 2-3 minutes after vigorous mixing. **(C)** Fractional area of the condensed phase as calculated from Fiji-ImageJ software as a function of [T]/[Arg] ratio. **(D)** Partition coefficient of dT40 and [RGRGG]₅ as a function of [T]/[Arg] ratio.
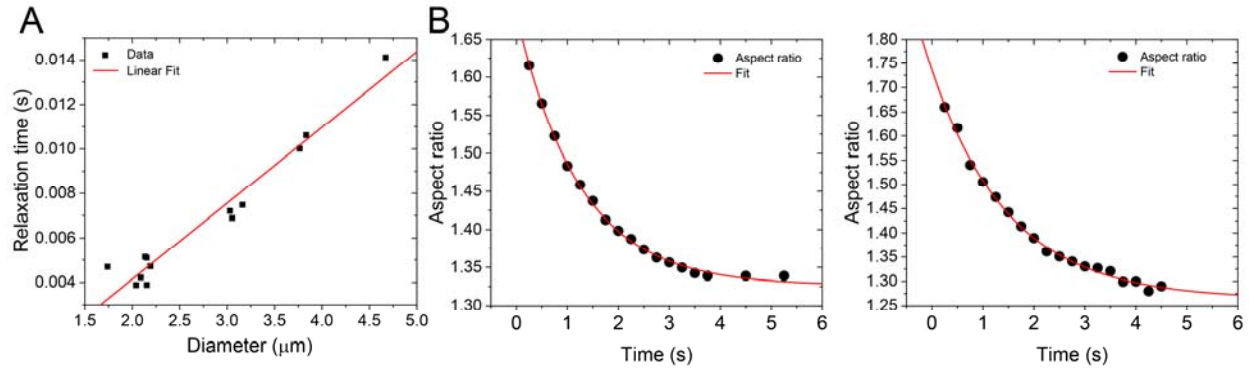
Fig. S2. Determination of inverse capillary velocity: (A) Active fusion: Linear relation between the fusion-relaxation time and the diameter of the condensates for the active fusion of suspended droplets using a dual-trap optical tweezer. The relaxation time is obtained from the laser signal as trapped condensates undergo fusion (see Fig. 1B in the Main-text). The slope of the linear fit represents the scaled relaxation time which is proportional to the ratio of η/γ (see Equation-1, Main-text). **(B) Passive fusion:** Aspect ratio analysis of two instances of passive fusion of two condensates on a tween-coated glass coverslip surface (see Movies S1 and S2). These condensates were prepared identically as in Fig. S2A for our active fusion assay. The exponential fits give a normalized relaxation time of ~100 ms/µm, which is more than one order of magnitude higher than the same obtained from OTF experiments (~3.4 ms/µm). These data indicate a dominant role of surface drag force during passive droplet fusion on a microscope coverslip for these condensates.
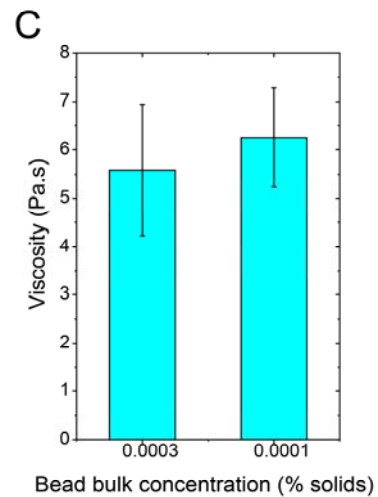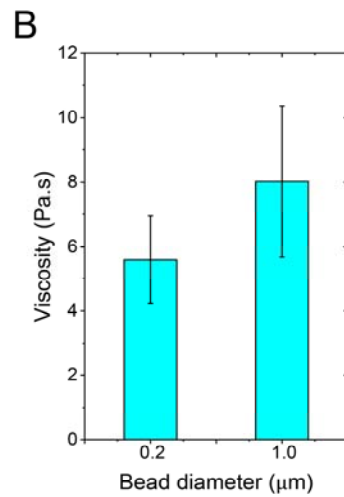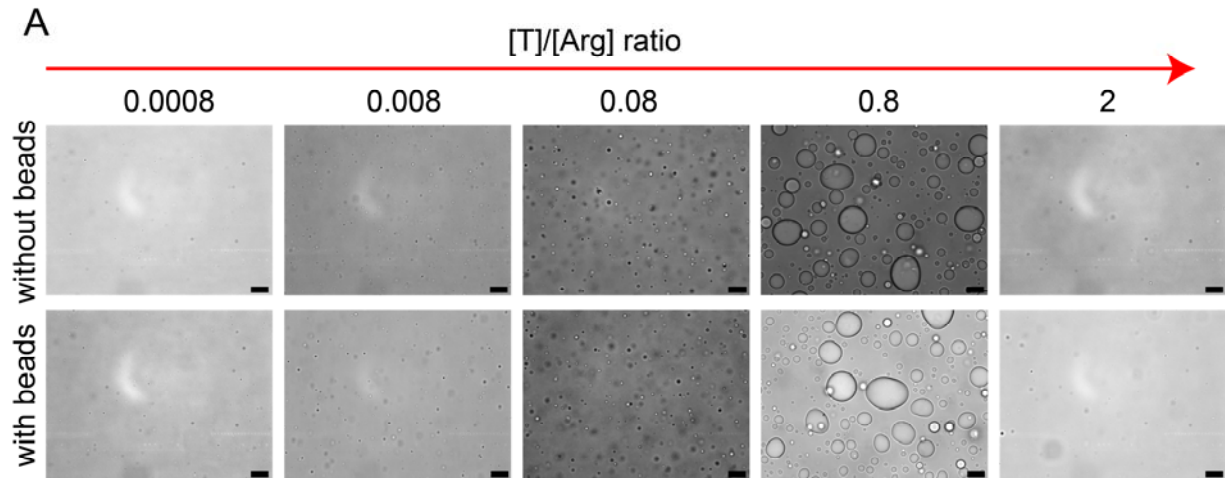
Fig. S3. (A) Bright-field microscopy images for [RGRGG]$_5$-dT40 condensates in the presence and absence of beads. Scale bar represents 10 μm. **(B)** Viscosity of [RGRGG]$_5$-dT40 condensates prepared at [Arg]/[T]=0.4 as determined by particle tracking of two bead diameters; 0.2 and 1.0 μm. **(C)** Viscosity of [RGRGG]$_5$-dT40 condensates prepared at [Arg]/[T]=0.4 for different bead concentrations.
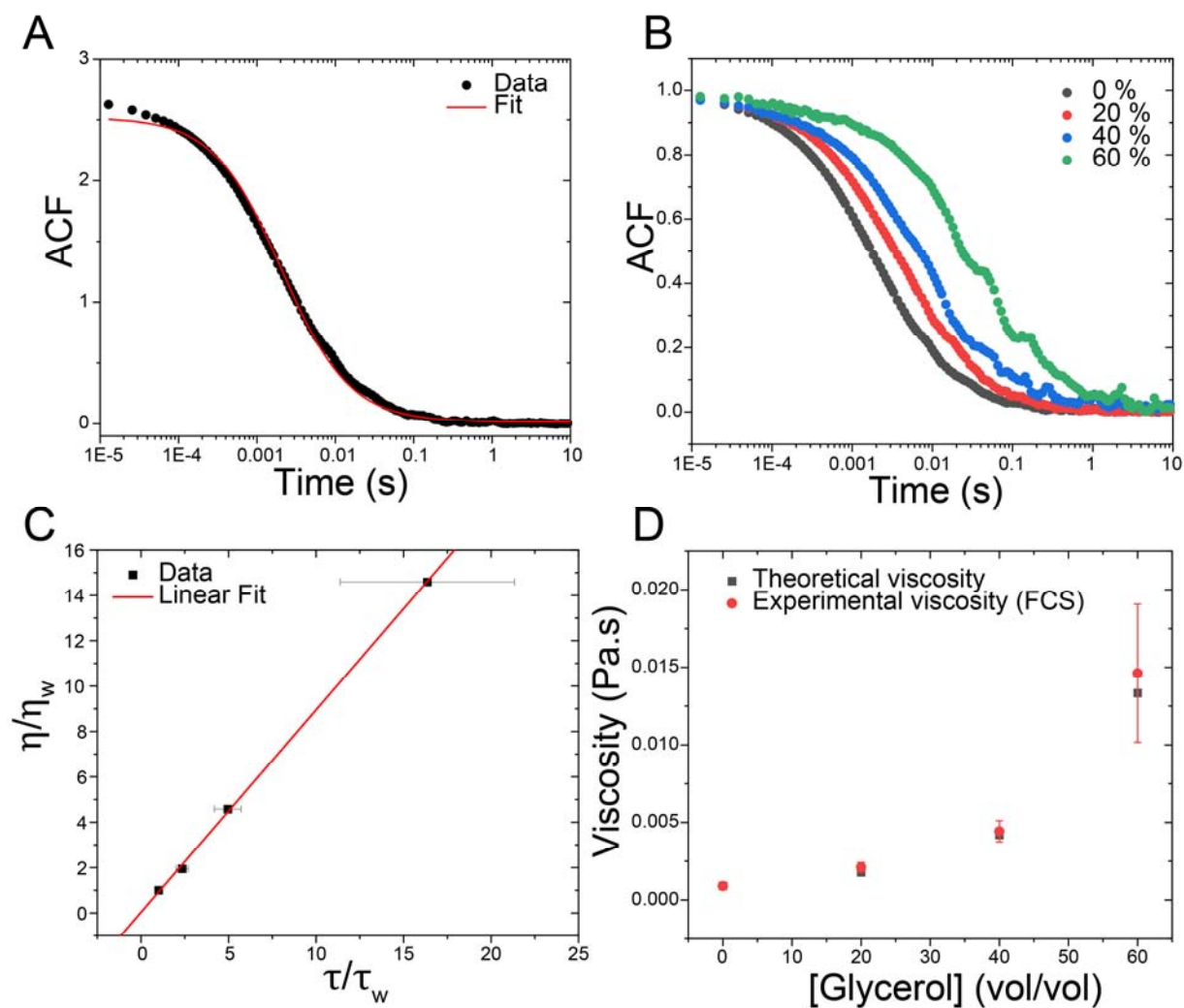
Fig. S4. Diffusion of 20 nm beads in glycerol/water mixtures as measured by FCS. (A) Autocorrelation function and fit for 20 nm bead diffusion in water. **(B)** Autocorrelation functions of the same beads in glycerol/water mixtures. **(C)** Viscosity and diffusion time normalized by their respective values in water showing a linear correlation, consistent with what was previously found in Sherman et al[19]. **(D)** Measured viscosity calculated from the Stoke-Einstein equation and the FCS-derived diffusion coefficient overlaid on the expected viscosity of glycerol/water mixtures as calculated by the formula reported in the literature[20,21], which were also compared with published experimental results[22].
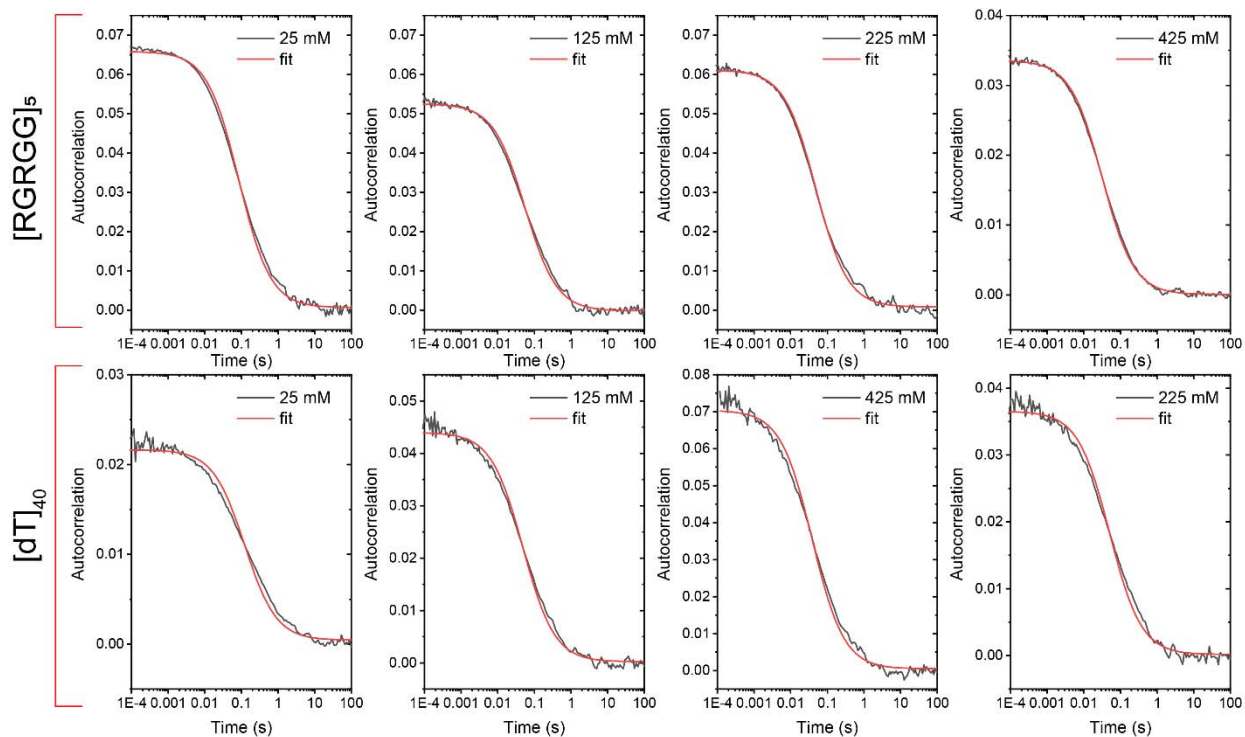
Fig. S5. Representative FCS autocorrelation curves for Atto488-dT40 and Alexa594-[RGRGG]$_5$ within [RGRGG]$_5$-dT40 condensates at various salt (NaCl) concentrations. The top row corresponds to the autocorrelation curves for Alexa594-[RGRGG]$_5$ diffusion within the condensates. The bottom row corresponds to the autocorrelation curves for Atto488-dT40 diffusion within the condensates. The red lines are fits of Equation-3 (see *Fluorescence correlation spectroscopy* section in Methods).
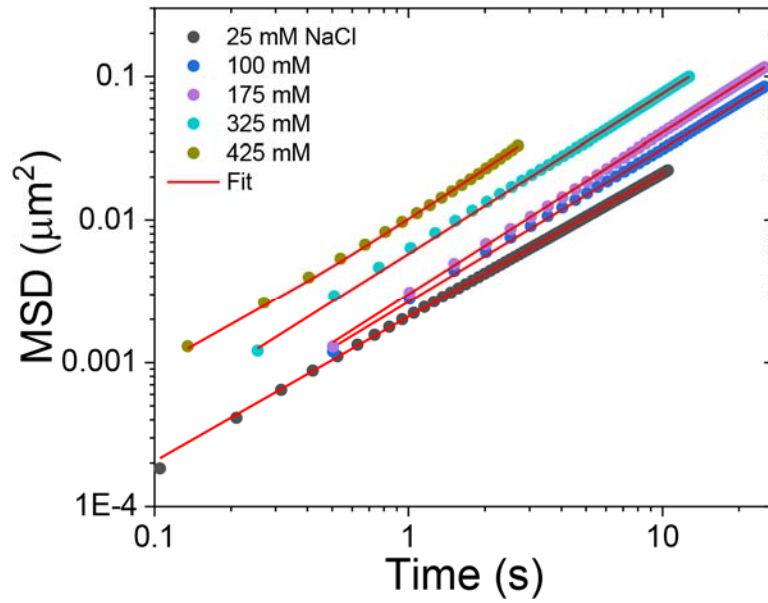
Fig. S6. Ensemble-averaged mean squared displacement (MSD) as a function of increasing salt concentration for 200 nm beads within [RGRGG]$_5$-dT40 condensates prepared at a ratio of [T]/[Arg] = 0.40. The red lines are fits of Equation-2 added to a constant (See *video particle tracking microscopy* section in Methods).
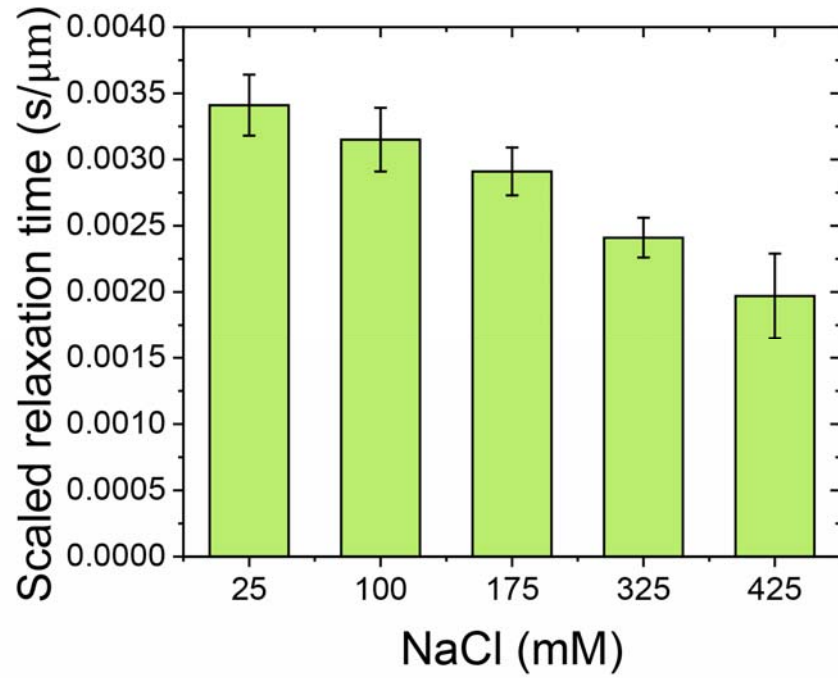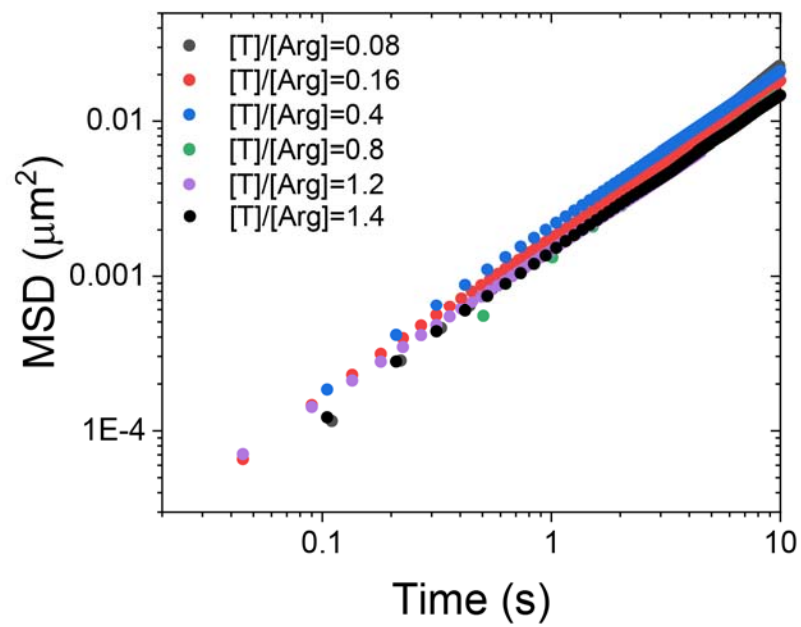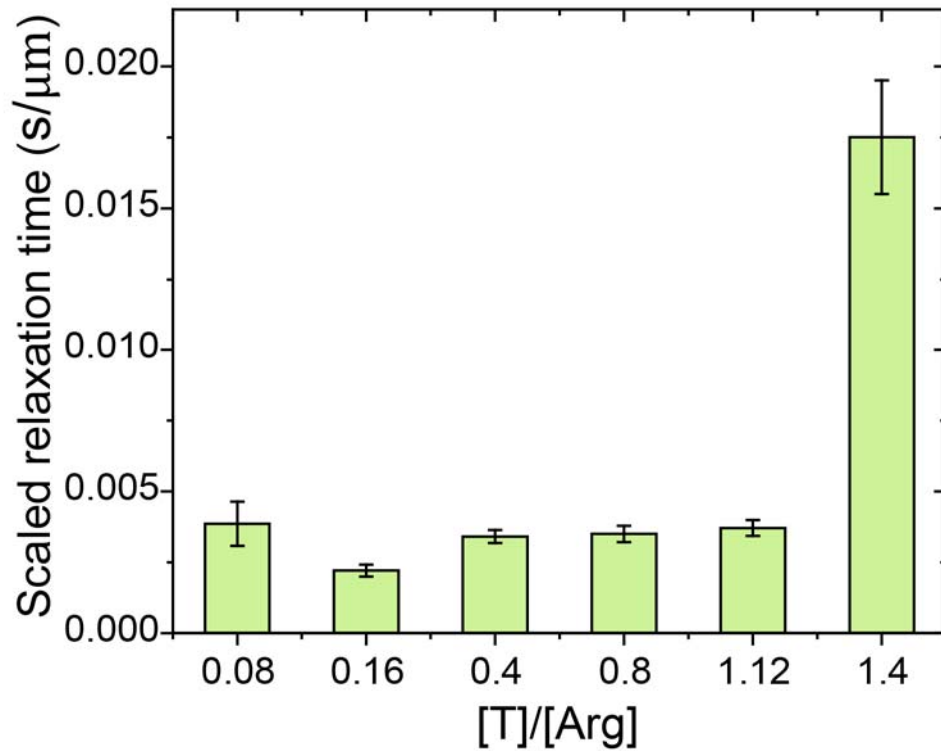
Fig. S7. Scaled fusion relaxation time for [RGRGG]$_5$-dT40 condensates, prepared at various salt concentrations, using our OTF assay.
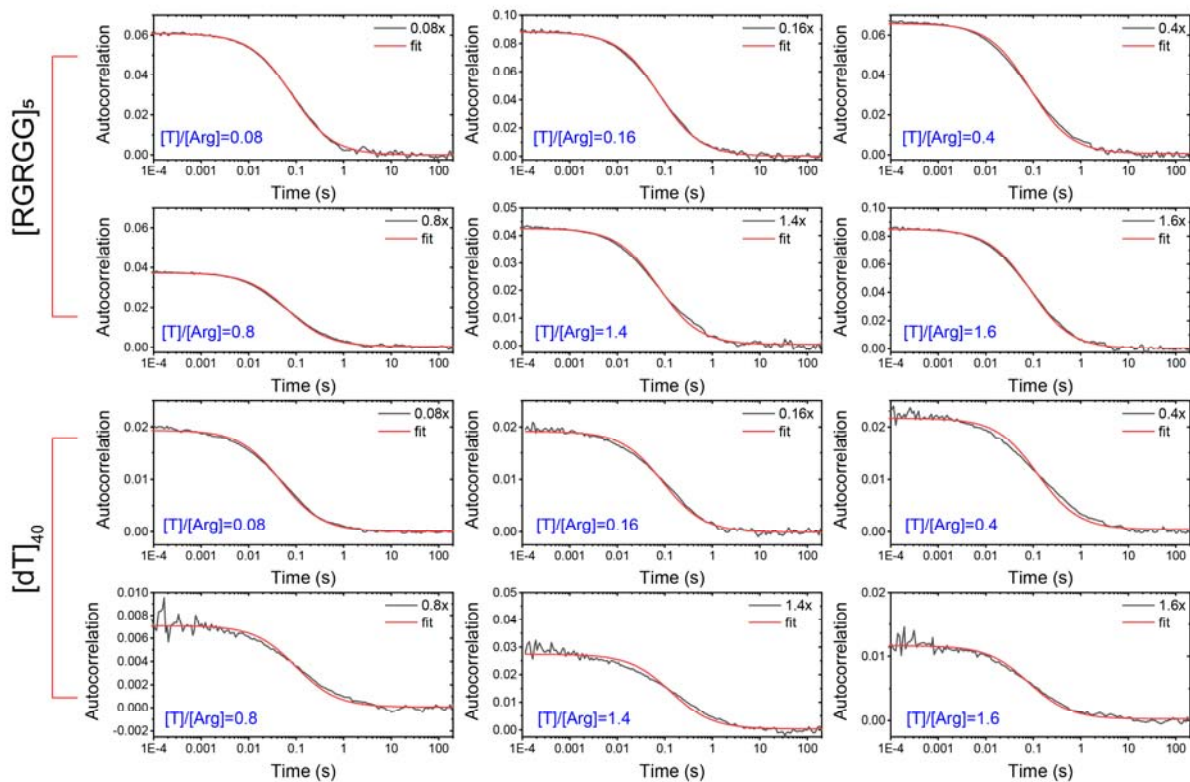
Fig. S8. Representative FCS autocorrelation curves for Atto488-dT40 and Alexa594-[RGRGG]₅ within [RGRGG]₅-dT40 condensates at various mixing ratios. The top two rows correspond to the autocorrelation curves of Alexa594-[RGRGG]₅ within these condensates. The bottom two rows show autocorrelation curves for Atto488-dT40 within these condensates. The red lines are fits of Equation-3 (see *Fluorescence correlation spectroscopy* section in Methods).

Fig. S9. Ensemble-averaged mean squared displacements (MSD) of 200 nm beads within [RGRGG]$_5$-dT40 condensates at variable [T]/[Arg] mixing ratios as indicated.

Fig. S10. Scaled fusion relaxation time of [RGRGG]$_5$-dT40 condensates, prepared at different [T]/[Arg] molar ratios, from our OTF assay. For higher [T]/[Arg] ratios (*e.g.* [T]:[Arg] = 1.6), we observed that droplets do not fuse (see Movies S3&S4 and Figure 3E in the Main-text).
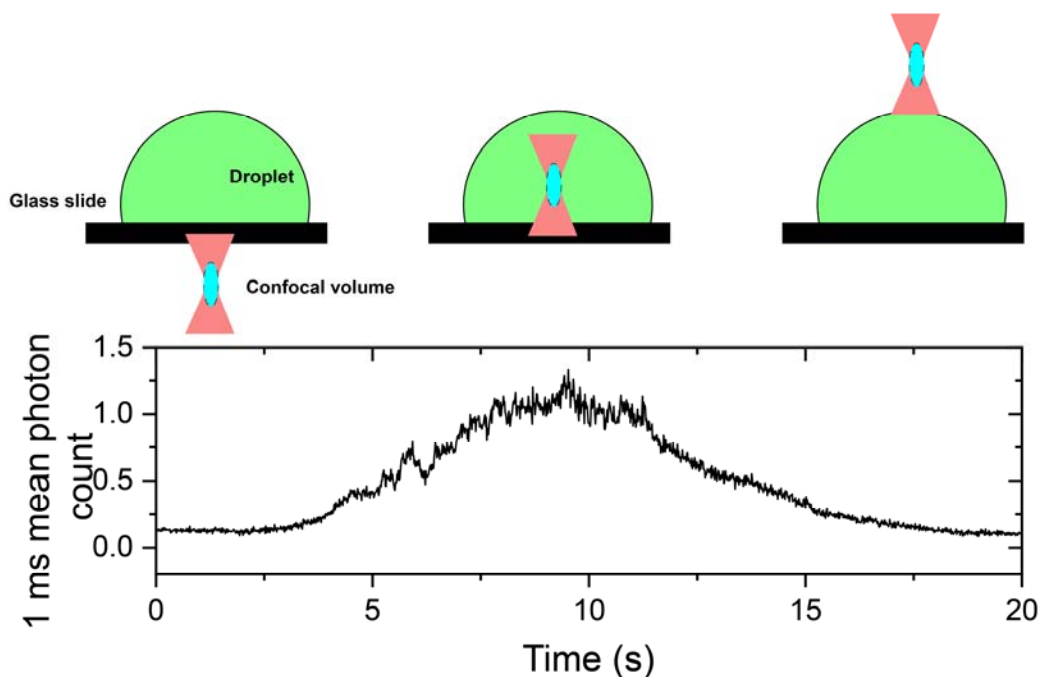
Fig. S11. Point Z-scan at the center of a [RGRGG]$_5$-dT40 condensate. The confocal volume is initially placed on the glass slide surface where only photons from the background are detected. The nanostage of the microscope was then set to move in the Z-direction in steps of 200 nm and three steps per second. The Z-location of the nanostage that corresponds to the maximum intensity is chosen for FCS measurements. Condensates that were large enough (~ 15 µm in diameter) were considered for FCS measurements. This is to ensure that the location of the confocal volume is ≥ 6 µm above the glass surface.
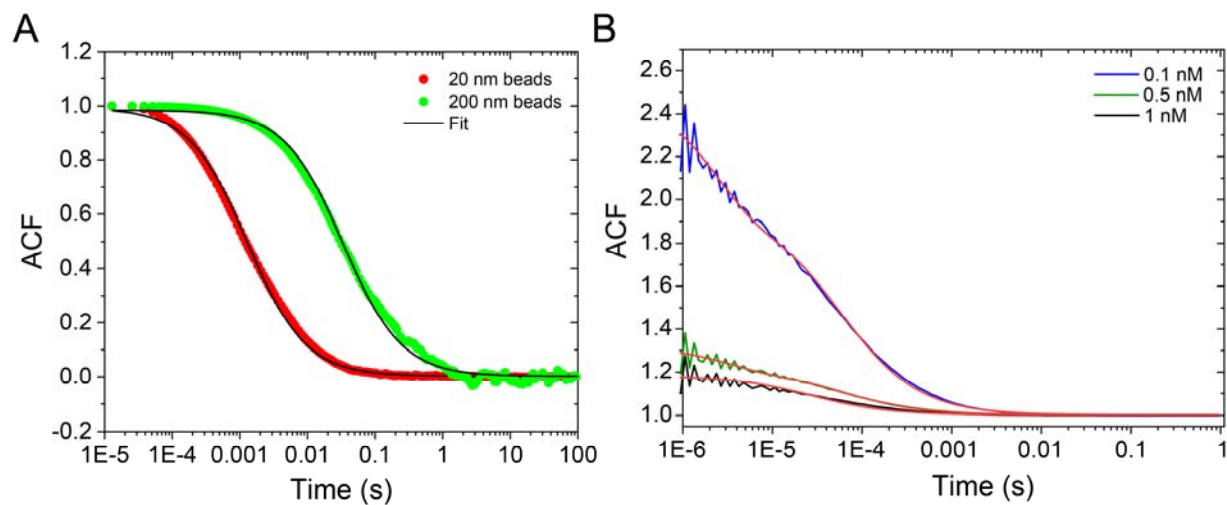
Fig. S12. (A) Autocorrelation curves for the diffusion of 20 nm beads and 200 nm beads in water as measured by FCS. **(B)** Autocorrelation and fits for the diffusion of free Alexa-488 dye in water. The fits in **(B)** are using Equation-3 with a triplet state term[23]. The fits in **(A)** are using Equation-3 (see *Fluorescence correlation spectroscopy* section in Methods).
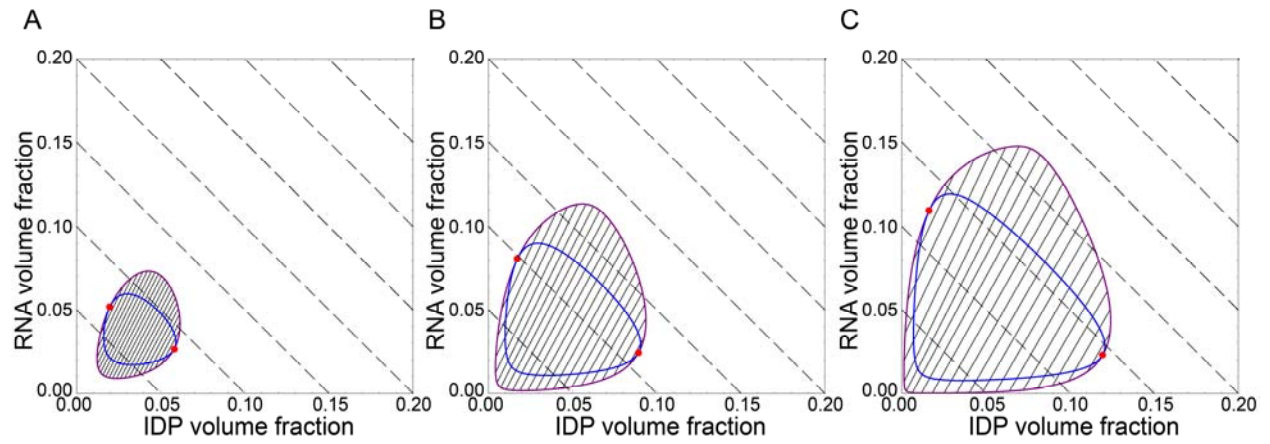
Fig. S13. Computed model phase diagrams showing that the extent of the calculated closed-loop two-phase regime is sensitive to increasing NA-IDP attraction strength. Parameters used were γ_1 = 100, γ_2 = 370, w_{11} = 0.4, w_{22} = -0.3 for all panels, while in **(A)** w_{12} = -2.2, **(B)** w_{12} = -2.27, **(C)** w_{12} = -2.35. [IDP: Intrinsically disordered polypeptide].

Supporting References

1 Alshareedah, I. *et al.* Interplay between Short-Range Attraction and Long-Range Repulsion Controls Reentrant Liquid Condensation of Ribonucleoprotein–RNA Complexes. *Journal of the American Chemical Society* **141**, 14593-14602, doi:10.1021/jacs.9b03689 (2019).

2 Banerjee, P. R., Moosa, M. M. & Deniz, A. A. Two-Dimensional Crowding Uncovers a Hidden Conformation of α-Synuclein. *Angewandte Chemie* **128**, 12981-12984 (2016).

3 Banerjee, P. R. & Deniz, A. A. Shedding light on protein folding landscapes by single-molecule fluorescence. *Chemical Society Reviews* **43**, 1172-1188 (2014).

4 Banerjee, P. R., Milin, A. N., Moosa, M. M., Onuchic, P. L. & Deniz, A. A. Reentrant Phase Transition Drives Dynamic Substructure Formation in Ribonucleoprotein Droplets. *Angew Chem Int Ed Engl* **56**, 11354-11359, doi:10.1002/anie.201703191 (2017).

5 Banerjee, P. R., Mitrea, D. M., Kriwacki, R. W. & Deniz, A. A. Asymmetric Modulation of Protein Order-Disorder Transitions by Phosphorylation and Partner Binding. *Angew Chem Int Ed Engl* **55**, 1675-1679, doi:10.1002/anie.201507728 (2016).

6 Kaur, T. *et al.* Molecular Crowding Tunes Material States of Ribonucleoprotein Condensates. **9**, 71 (2019).

7 Patel, A. *et al.* A Liquid-to-Solid Phase Transition of the ALS Protein FUS Accelerated by Disease Mutation. *Cell* **162**, 1066-1077, doi:https://doi.org/10.1016/j.cell.2015.07.047 (2015).

8 Alshareedah, I., Kaur, T. & Banerjee, P. R. in *Methods in Enzymology*   (Academic Press, 2020).

9 McGlynn, J. A., Wu, N. & Schultz, K. M. Multiple particle tracking microrheological characterization: Fundamentals, emerging techniques and applications. *Journal of Applied Physics* **127**, 201101 (2020).

10 Tinevez, J.-Y. *et al.* TrackMate: An open and extensible platform for single-particle tracking. *Methods* **115**, 80-90 (2017).

11 Allan, D. et al., DOI: 10.5281/zendo.60550 (2019).

12 Paul Müller (2012) *Python multiple-tau algorithm* (Version 0.1.9). Available at https://pypi.python.org/pypi/multipletau/ (Accessed 15 Sep 2020).

13 see pycorrelate documentation at https://pycorrelate.readthedocs.io/en/latest/.

14 Enderlein, J., Gregor, I., Patra, D., Dertinger, T. & Kaupp, U. B. Performance of fluorescence correlation spectroscopy for measuring diffusion and concentration. *ChemPhysChem* **6**, 2324-2336 (2005).

15 Rüttinger, S. *et al.* Comparison and accuracy of methods to determine the confocal volume for quantitative fluorescence correlation spectroscopy. *Journal of microscopy* **232**, 343-352 (2008).

16 Schindelin, J. *et al.* Fiji: an open-source platform for biological-image analysis. *Nature methods* **9**, 676 (2012).

17 Dobkin, D. P., Wilks, A. R., Levy, S. V. F. & Thurston, W. P. Contour tracing by piecewise linear approximations. *ACM Transactions on Graphics* **9**, 389–423, doi:10.1145/88560.88575 (1990).

18 W.P. Thurston, personal communication.

19 Sherman, E. *et al.* Using fluorescence correlation spectroscopy to study conformational changes in denatured proteins. *Biophysical journal* **94**, 4819-4827 (2008).

20 Cheng, N.-S. Formula for the viscosity of a glycerol− water mixture. *Industrial & engineering chemistry research* **47**, 3285-3288 (2008).

21 Volk, A. & Kähler, C. J. Density model for aqueous glycerol solutions. *Experiments in Fluids* **59**, 75 (2018).

22   Segur, J. B. & Oberstar, H. E. Viscosity of glycerol and its aqueous solutions. *Industrial & Engineering Chemistry* **43**, 2117-2120 (1951).
23   Widengren, J., Mets, U. & Rigler, R. Fluorescence correlation spectroscopy of triplet states in solution: a theoretical and experimental study. *The Journal of Physical Chemistry* **99**, 13368-13379 (1995).